Landslide Susceptibility Mapping of the Kuchisakamoto Area, Central Japan using DTM from Airborne LIDAR

Hiroshi P. SATO and Tatsuo SEKIGUCHI

Abstract

Detailed understanding of landslide susceptibility mapping is important if effective measures against landslides are to be taken. The Kuchisakamoto area in Shizuoka City, central Japan, has suffered from frequent landslides. Conventional techniques can only measure the detailed terrain in vegetated areas with difficulty. Airborne light detection and ranging (LIDAR) is a promising tool to precisely and directly measure a digital terrain model (DTM). Using a five-meter-grid DTM we attempted to map landslide susceptibility. In advance, we prepared a landslide inventory map, and cells were separated into landslide and non-landslide cells. First, we calculated the terrain slope and upstream drainage area of each cell. These are the important factors inducing landslides in Japan. Secondly, these parameters were classified into 48 sections, and the landslide density, which is the number of landslide cells divided by the total number of cells, was calculated for each section. The landslide density was classified into four categories, such as very low (0-1 % in the density), low (1-5 %), high (5-10 %), very high (>10 %), and finally, landslide susceptibility was mapped based on the four categories. The obtained landslide susceptibility is believed to be able to predict the severity of disaster in the study area.

1. Introduction

Japan is subject to tectonic movements which render its topographical features easily eroded. Furthermore, since Japan is located in a warm-humid climatic region, the high precipitation promotes active mass movements (Ohmori, 2000). Earthquake-induced and rain-induced landslides may cause disastrous damage to houses and buildings.

In the 1995 Hyogo-ken Nanbu Earthquake, landslides occurred in and around Kobe City, Hyogo Prefecture, Japan (Fukuoka et al., 1997). On July 20, 2003, debris flow took place in Minamata City, Kumamoto Prefecture, Japan, triggered by the heavy rainfall (Sassa et al., 2004).

To avoid such disasters in the future, it is necessary to scientifically assess the areas susceptible to landslides (Lee et al., 2003). Until now, photogrammetry has been used to produce contour maps and the landslides which caused these disasters, have been investigated using these maps. It is important to understand the fundamental mechanism of landsliding by using contour maps which show the internal deformation features in landslides in detail. It has recently become possible to use a new technology called airborne light detection and ranging (LIDER) for direct and detailed measurement of the digital terrain model (DTM). Investigators have begun to extract airborne LIDAR to identify geomorphological and topographical characteristics in landslide areas.

For example, Sekiguchi and Sato (2004) reported that contour maps from airborne LIDAR-DTM had been useful producing a landslide inventory and micro-topographic classification map in the Tama Hills, near Tokyo, Japan. McKean and Roering (2004) used DTM derived from airborne LIDAR to quantify the local surface roughness of a landslide complex near Christchurch, New Zealand. It is expected that LIDAR will accelerate high-precision topographic mapping and detailed landform analysis. In this study we describe the principle of this new technology and we show examples of landslide susceptibility mapping using DTM from airborne LIDAR.

Table 1 Meteorological data in 2002, near the study area.

	Precipitation (mm)			Temperature (℃)			Sunshine duration (hr)
	Monthly	Daily highest	Hourly highest	Mean	Highest	Lowest	
Jan.	185.0	109.0	23.0	2.0	15.5	-6.7	160.8
Feb.	53.0	23.0	4.0	2.6	13.0	-5.6	154.1
Mar.	261.0	96.0	12.0	6.8	17.6	-3.4	183.3
Apr.	108.0	29.0	6.0	11.5	23.8	1.9	138.9
May	229.0	52.0	10.0	14.1	25.9	6.9	116.4
Jun.	229.0	45.0	12.0	17.4	27.1	10.0	106.0
Jul.	713.0	450.0	83.0	22.9	32.0	15.5	158.6
Aug.	88.0	44.0	9.0	22.6	32.2	15.8	190.1
Sep.	246.0	79.0	14.0	18.4	29.7	10.0	113.1
Oct.	75.0	75.0	26.0	13.0	25.9	1.2	170.1
Nov.	28.0	28.0	8.0	6.3	17.3	-1.5	157.7
Dec.	37.0	37.0	7.0	3.4	13.8	-4.8	135.5

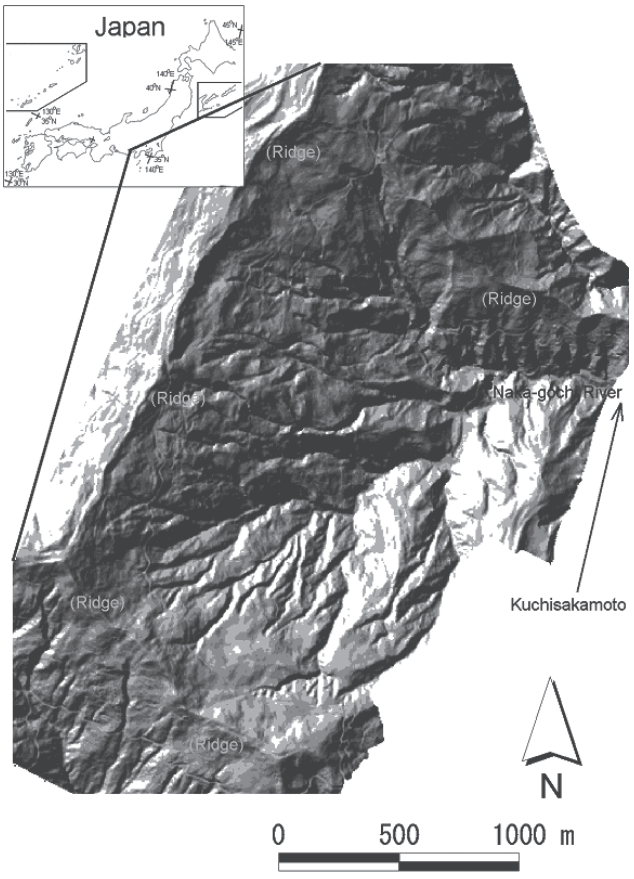

Fig. 1 Study area.

2. Study area

The study area is located in the Kuchisakamoto area, in Shizuoka City, central Japan (Fig. 1). It extends for 2.2 km^2 and its altitude ranges from 550 m to 1,350m. It is mainly covered with artificially planted needle-leaf evergreen forest.

The meteorological data near the study area are observed and recorded by the Japan Meteorological Agency (in Table 1). The annual mean precipitation is 3,120 mm/yr. The observation period at Ikawa observation station, located 6 km northwest of the study area, was the 22 years from 1979-2000. The meteorological data in 2002 are shown in Table 1. The seasonal changes are obvious. In summer the highest temperature is over 30℃ in summer, and in winter snowy days are rare but the lowest temperature is < 0℃. In summer and autumn, the study area is often subjected to heavy storms caused by typhoons and the shifting Polar Front. In Table 1 highest daily and hourly precipitations were 450.0 mm and 83.0 mm in July 10, 2002 when a typhoon hit the study area.

The geology of the study area is dominated by rhythmic alternated stratae of sandstone and shale, which are Paleogene marine sediments. Tectonic lines and a major fault line run near the study area, and tectonic movements have fractured these strata.

On April 5 and 6, 2001, the study area was measured by airborne LIDAR for the investigators experiment; aerial photographs were also taken at 1/8,000 scale at the same time (Hasegawa and Okamatsu, 2001).

Fig. 2 Study area.

Viewed through the stereoscope, the aerial photographs reveal many past landslides at the slope. For example, "A" in Fig. 2 where deciduous shrubs ca. 5 m in height and annual grasses 2 m in height grow instead of the needle-leaf evergreen trees.

When the DTM was measured by LIDAR, namely in the early spring, neither deciduous shrubs nor grasses had begun to grow. Furthermore, the needle-leaf evergreen forest was not so dense. As a result, the laser beam could scan and measure the terrain not only through the shrubs and grasses but also through the needle-leaf evergreen forest.

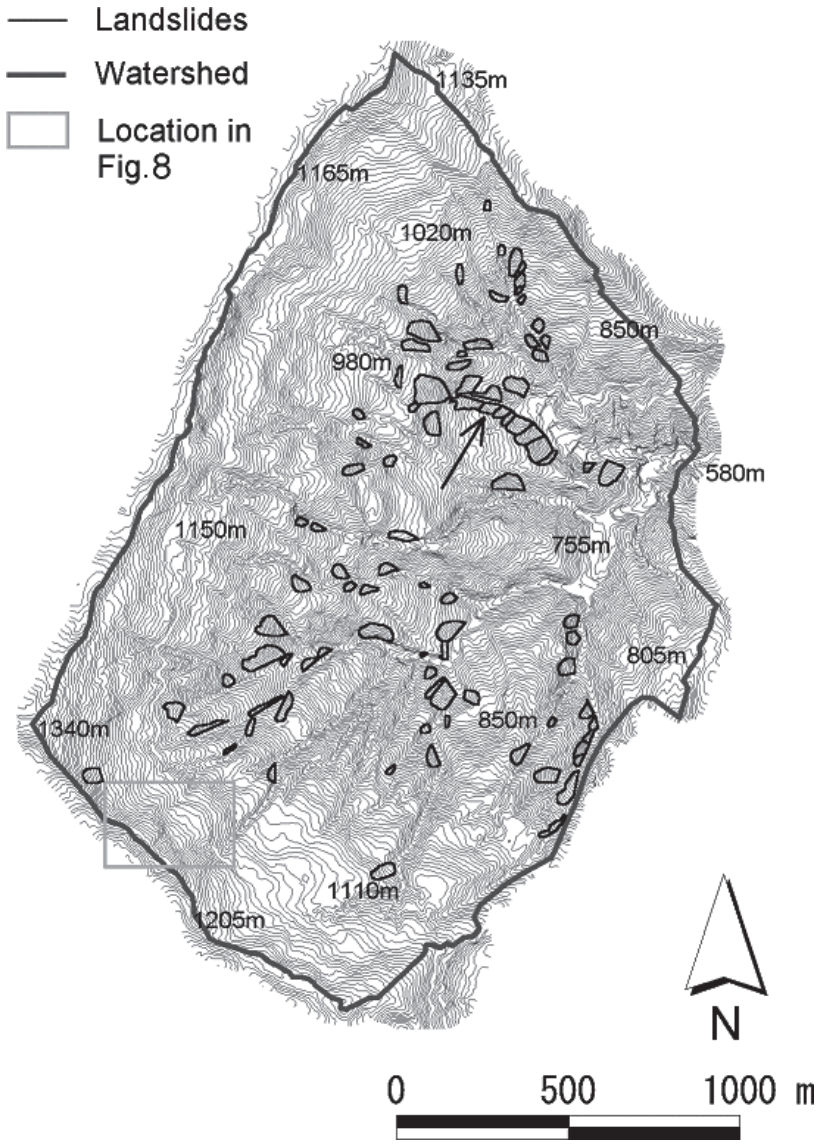

Fig. 3 Landslide inventory map in the study area.

In Fig. 3, the boundaries of the ninety identified landslides are delineated with the black lines. The largest watershed, which is 318.37 ha in area, is delineated in the bold dark gray line in the figure. In each landslide, a scar was clearly identified. However, it was difficult to identify the transportation and accumulation areas on the aerial photographs, because the surface of the landslides has been secondary eroded and the original internal deformation in the landslides no longer remains. The identified past landslides are from 15 m to 100 m wide.

Fig. 4 Close-up photograph of landslide which occurred on July 10, 2002.

The landslide shown in the Fig. 4 occurred on July 10, 2002. The position of the landslide is shown as the head of the arrow in Fig. 3, namely the landslide occurred at the same location as where the previous landslide was identified. In Fig. 4, the size of the landslide is 10 m in width, 20 m in slope length, and 5 m in depth. The shale was deeply weathered, ca. 5 m thick and had turned into brown soil at the upper slope of "A". At the middle slope of "B" ca. 2 cm-size-fractured black shale fragments appeared which piled up as talus cones at the lower slope. The fallen tree, which was from the artificially planted forest above "A", is identified below "B" in Fig. 4. More than 10 cm-size-fractured white sandstone blocks were also exposed and scattered at the lower slope ("C" in Fig. 4). Based on the above field survey this reactivated landslide is re-classified into a debris avalanche (Varnes, 1978; Hutchinson, 1988).

3. Airborne LIDAR-measurement

3.1 Airborne LIDAR

More information about Airborne LIDAR is available in Ackermann (1999), Wehr and Lohr (1999) and other articles in the same issue of the ISPRS Journal of Photogrammetry and Remote Sensing.

Described simply, airborne LIDAR is an aircraft-mounted electro-optical distance meter that measures the distance between an aircraft and the ground. Figure 5 shows the concept of DTM measurement by airborne LIDAR. Its development began in the 1970s and 1980s with an early U.S. National Aeronautics and Space Administration (NASA) system and various other attempts in the United States and Canada. It first became possible by using a pulse laser operating in the near-infrared, which provided clearly recordable return signals after diffusion and reflection from the ground (Ackermann, 1999).

Airborne LIDAR measurements offer the following advantages: 1) to obtain detailed DTM in digital form rapidly in comparison to digital photogrammetry; 2) to measure the ground under vegetative cover provided it is not too dense (Masaharu et al., 2001); 3) to obtain dense measurement points, for example, several points per square meter; and 4) to measure at night under conditions in which aircraft can fly safely. Daytime flying is undoubtedly safer but when a night-time landslide occurs and it is urgent to map the landform deformation, this advantage will be useful for rapid deployment of disaster rehabilitation activities.

If the laser beams were transmitted in only one direction, the reflected points on the ground would all lie on a line along the flight path. Hence, the aircraft might have to flight many different courses to cover the whole study area. In practice, using a swinging mirror mounted in front of the laser transmitter and receiver, the laser beams are reflected to the cross-flight directions (Fig. 5) and the sensor can measure many points not only in the flight direction but also in a cross-flight direction; as a result the sensor can cover the whole study area much more efficiently.

Describing the principle more closely, the airborne LIDAR sensor is an active sensor that measures

the distance from the sensor to the target from which the laser beam is reflected. The onboard Global Positioning System (GPS) and Inertial Measurement Unit (IMU) measure position and attitude of the sensor, respectively. The scanning angle of the mirror is also simultaneously measured on the aircraft. The three-dimensional positions of ground targets are obtained by combining these data with measured distances from the sensor (Masaharu et al., 2001).

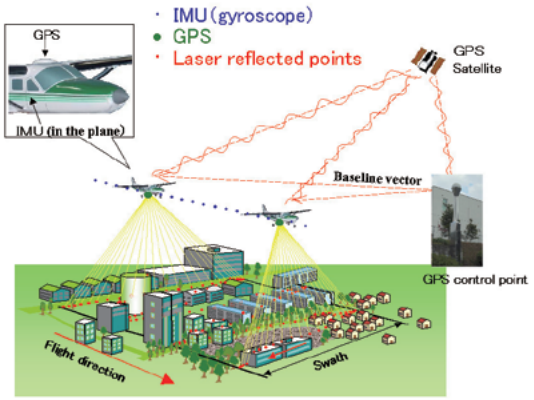

Fig. 5 Concept of the airborne LIDAR

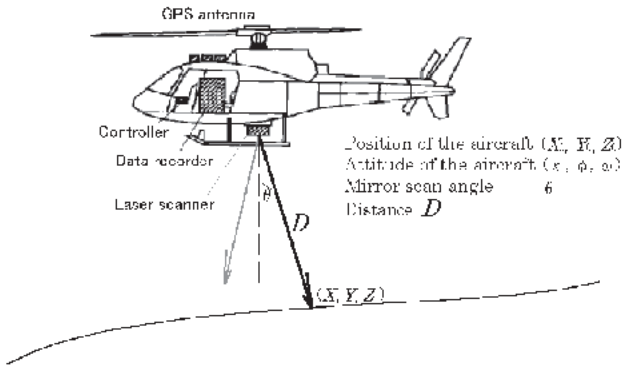

Fig. 6 Relation between the positions of an aircraft and a laser reflected point (Masaharu et al., 2001, modified).

As in Fig. 6, when the aircraft position is (X_0, Y_0, Z_0), and the attitude of the aircraft is (κ, φ, ω), the distance separating the aircraft and the target is D, scanning angle of the mirror is θ (the direction directly below the aircraft is zero), and the target position on the ground (X, Y, Z) is calculated as

$$\begin{pmatrix} X \\ Y \\ Z \end{pmatrix} = \begin{pmatrix} X_0 \\ Y_0 \\ Z_0 \end{pmatrix} + \mathbf{R}_Z \mathbf{R}_Y \mathbf{R}_X \mathbf{R}_m D \begin{pmatrix} 0 \\ 0 \\ -1 \end{pmatrix}. \quad (1)$$

Here, $\mathbf{R}_Z$, $\mathbf{R}_Y$, $\mathbf{R}_X$, and $\mathbf{R}_m$ are

$$\mathbf{R}_Z = \begin{pmatrix} \cos\kappa & -\sin\kappa & 0 \\ \sin\kappa & \cos\kappa & 0 \\ 0 & 0 & 1 \end{pmatrix} \quad (2)$$

$$\mathbf{R}_Y = \begin{pmatrix} \cos\phi & 0 & \sin\phi \\ 0 & 1 & 0 \\ -\sin\phi & 0 & \cos\phi \end{pmatrix} \quad (3)$$

$$\mathbf{R}_X = \begin{pmatrix} 1 & 0 & 0 \\ 0 & \cos\omega & -\sin\omega \\ 0 & \sin\omega & \cos\omega \end{pmatrix} \quad (4)$$

$$\mathbf{R}_m = \begin{pmatrix} 1 & 0 & 0 \\ 0 & \cos\theta & -\sin\theta \\ 0 & \sin\theta & \cos\theta \end{pmatrix}. \quad (5)$$

An Optech ALTM1225 instrument was used in this study. The measurement resolution was 4 points per square meter. Table 2 shows actual measurement parameters that were decided in consideration of a safety factor (Hasegawa and Okamatsu, 2001). In Table 2, the pulse rate (Hz) indicates the number of times the laser pulses are transmitted per second; scanning frequency (Hz) indicates the rate of the mirror's swinging per second. The measurement density is dependent on the pulse rate, the scanning frequency, the flight altitude, and aircraft speed.

3.2 First and last pulses

When the laser beam is transmitted directly below the instrument and reflected on the terrain surface, it leaves a round "footprint" on the ground (Fig. 7).

In Table 2, a flying altitude of 600 m and beam divergence of 0.3 mrad produces an 18-cm-diameter "footprint". The beam is reflected first from the tree

canopy, next, inside the tree, lastly, from the ground (Fig. 7). The first reflected beam is called the 'first pulse'; the final reflected pulse is called the 'last pulse'. Other reflected pulses are called simply 'other pulses'. The reflected pulse is received and recorded by the onboard receiver and recorder. The first pulse is received earlier than the other pulses, and the other pulses are received earlier than the last pulse. These difference pulses are identified by the time lag.

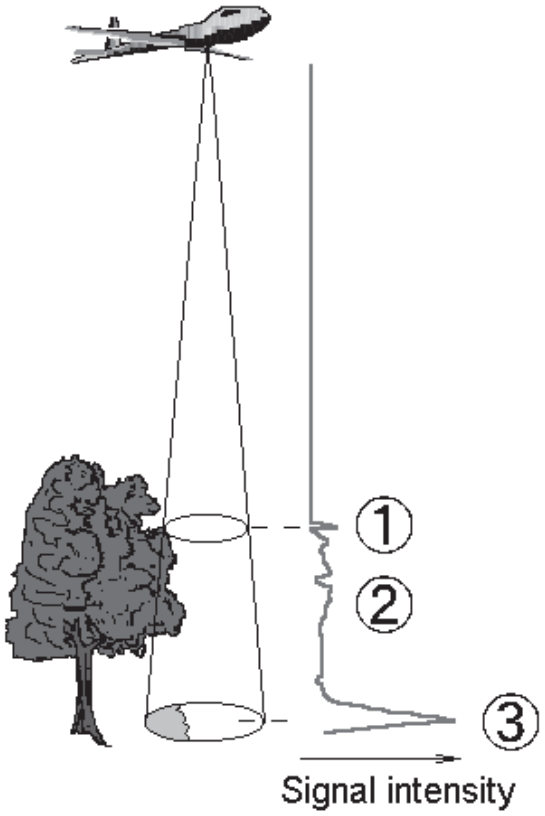

Fig. 7 Relation between vegetation and return signal: 1, first pulse; 2, other pulses; 3, last pulse.

In this study return signals from both the first and last pulses were received (Table 2). When the laser beam can penetrate fully into the canopy, the last pulse may be reflected on the ground. But when it cannot penetrate into the dense canopy, the last pulse may be reflected on trees. The points on the trees were filtered out to select only the point data on the terrain surface, namely, DTM. Initially, this filtering was done automatically. Briefly explaining, the study area was subdivided into the search areas, and the points in each search area are approximated by quadratic polynomials, which gave a threshold value from 2 m to 9 m. Those measurement points over the threshold value were eliminated from the original data. Later this filtering was done by manual inspection (Raber et al., 2002). The obtained DTM comprises x, y, and z coordinates of randomly distributed points. Five-meter-grid DTM was generated by interpolating the available original points, using the Inverse Distance Weighted (IDW) method (order: one; radius: five meters).

Table 2 Measurement parameters applied in this study by Optech ALTM1225. (Hasegawa and Okamatsu, 2001, modified)

Pulse rate	25,000 Hz
Scanning frequency	35 Hz
Mirror scan angle	12°
Measurement mode	Simultaneous first / last pulse mode observation
Measurement density	4 points/m^2
Footprint	18 cm in diameter
The number of flight course	15 courses
Overlap ratio between two courses	50%
Flying altitude	600 m above the ground
Flight speed	180 km/hr
Beam divergence	0.2 mrad

3.3 Measurement precision

In this study, the measurement precision was checked in several checking areas, containing laser reflected points measured during two adjacent flight courses. The checking method is as follows (Sato et al., 2002); Reflected points measured by one flight course were gathered, and the average elevation was calculated. In a second run, the average elevation was calculated based on another flight course. The discrepancy between the two average elevations was 0.06 m. Contours were obtained from reflected points measured by one flight course. To compare, contours were obtained from another flight course. Here the discrepancy between the two contour lines was 0.33 m in X, and –0.88 m in Y on average.

The several checking areas were measured twice, and discrepancy was also checked in the same way as the

above method. As a result, it was 0.05 m in X, –0.04 m in Y, and –0.01 m in Z on average. These figures provide an overview of the airborne LIDAR measurement precision achieved in this study.

3.4 Topography measured by airborne LIDAR

Different representations, including shaded relief maps, slope gradation maps, and contour maps can be used to show topography described by DTM. The shaded relief map shown in Fig. 1 was derived from the five-meter-grid DTM of Airborne LIDAR. The contour map shown in Fig. 3 was also obtained from the DTM.

Both airborne LIDAR and photogrammetric contour maps in the southwestern portion of the study area are shown in Fig. 8.

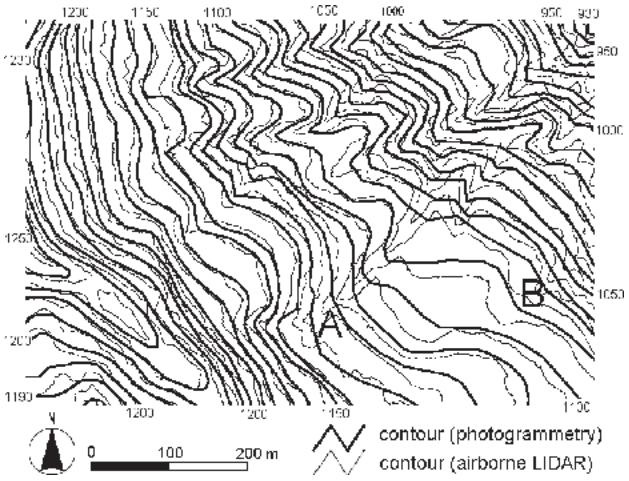

Fig. 8 Comparison of airborne LIDAR and photogrammetric contour maps (Sato et al., 2002).

The photogrammetric map reveals a smoother topography than the airborne LIDAR map. Using photogrammetric techniques, the contour lines can be obtained directly. Since the five-meter-grid DTM was obtained through interpolation, it may contain more noise than the photogrammetric map. However, based on the interpretation of aerial photographs and the field survey, it was found that valleys and other geomorphological features could be seen in better detail in the airborne LIDAR contour map than in the photogrammetric contour map.

For example, in Fig. 8, the valleys “A” and “B” in the LIDAR contours were confirmed by the field survey, but these gullies are not fully described by photogrammetric contours.

4. Landslide susceptibility mapping

It is difficult to identify slopes susceptible to landslides, because the latter are influenced by numerous factors such as lithology, geological structure, hydrology, topography, climate, vegetation, seismicity, and erosion (Hutchinson, 1988).

This study tried to identify landslide susceptibility by only topographic factors using five-meter-grid DTM from airborne LIDAR. Various topographic features have been calculated from grid DTM in the previous landslide studies. For example, McKean and Roering (2004) used a laplacian model to calculate in a three cells-by-three cells window of three-meter-grid DTM, and they evaluated spatial patterns of roughness in the landslide. Lee et al. (2002) calculated terrain slope and aspect from 200-meter-grid DTM for landslide susceptibility analysis.

To map landslide susceptibility, the terrain slope and upstream drainage area were considered in this study. The steeper the terrain slope, the more the soil layer is destabilized. The more the surface water and groundwater are collected in the upstream drainage area, the easier will the soil layer and deep soil stratum be fluidized. These two factors seem to be crucial in inducing landslides.

4.1 Terrain slope and upstream drainage area

4.1.1 Hatano’s contour map based method

Hatano (1974) investigated the relation between terrain slope and upstream drainage area, which are measured on the contour map. In his paper, Hatano (1974) did not directly describe it but the measurement method seems to have been as follows. Terrain slopes of the landslides θ were measured in degrees at the point M (in Fig. 9) in the transportation area of the landslide.

Upstream drainage area from the point M was measured as A (m^2) (in Fig. 9). But the larger the landslide area is, the larger the upstream drainage area would be. To compare several landslides with each other, Hatano (1974) tried to normalize the upstream drainage area. Namely, the upstream drainage area was divided by

the width of the landslide L (m) (in Fig. 9), and he investigated the relation between $\tan\theta$ and A/L.

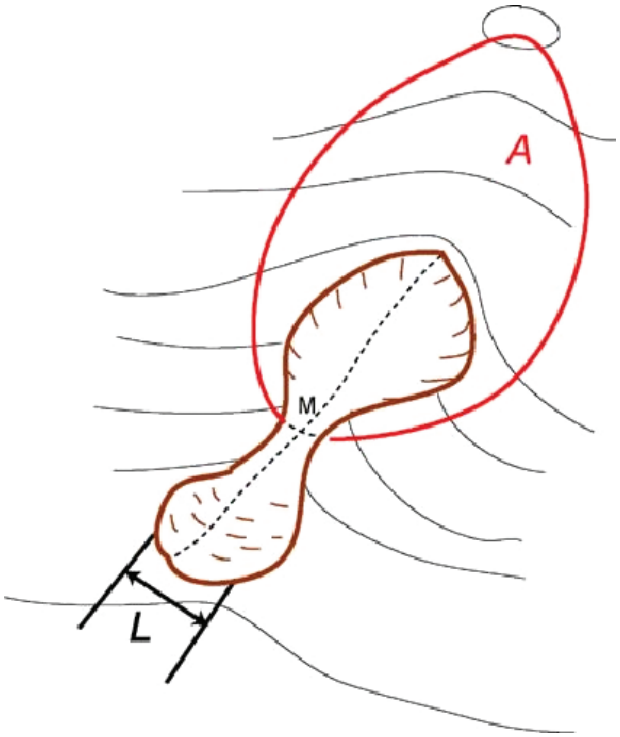

Fig. 9 Terrain slope and upstream measurement method by Hatano (1974).

In July 1973, a heavy downpour gave rise to several landslides in Amakusa-Kamishima in the Nagasaki Prefecture of Western Japan. Hatano (1974) selected fifteen of these whose width L (m) on the downstream side was 50 m or more, and plotted θ vs. A/L on log-log graph paper. Finally, he reported a correlation between $\tan\theta$ and A/L.

4.1.2 Grid DTM based method

In this study, these two parameters were calculated and investigated by using five-meter-grid DTM. In advance, past landslides were delineated by the polygons. In calculating A, a flow network such as Fig. 10 was also prepared in advance. The smallest upstream drainage area is one cell, namely, 25 m^2. The landslide width L was treated as constant with a value of five meters. This is because L is always five meters in the flow network and at the outlet of the past landslides polygons L is also always five meters. Hence, in this study A was directly treated instead of A/L.

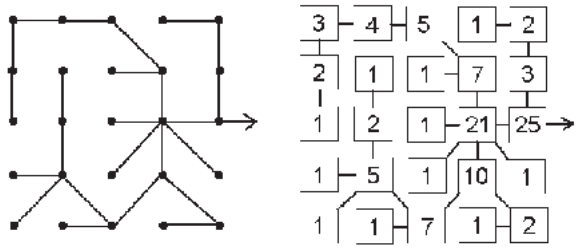

Fig. 10 Drainage network (left). Since the interval of the cells is five meters in this study, the right figure's number multiplied by 25 m^2 is the upstream drainage area at each cell.

Firstly, $\tan(\theta°)$ and A (m^2) at the center of the landslide were obtained. The center cells of the past landslides were picked up by the command "Centroid" of the Geographic Information System (GIS) software ArcInfo. Next, $\tan(\theta°)$ and A (m^2) of all non-landslide cells were obtained. Finally, $\tan\theta$ and A of landslide and non-landslide cells were plotted on log-log graph paper. The result is shown in the Fig. 11.

In the Fig. 11, the red dots show landslide center cells and blue dots show all non-landslide cells. There are 90 landslides in the study area and the number of the red dots was 90, and the number of the blue dots was 121,927. The total number of the cells was 122,017.

The two parameters on the red dots indicated the regression line in Fig. 11. For a given value of terrain slope, the larger the drainage area, the higher is the landslide susceptibility. When a certain value of drainage area is considered the steeper the terrain slope, the higher is the landslide susceptibility. The regression line is thought to indicate the average relation between terrain slope and drainage area in a past landslide, so that non-landslide cells at the upper part of the regression line would be mapped as higher landslide susceptibility locations than the non-landslide cells at the lower part. However, the correlation coefficient was poor, <-0.4, therefore, this mapping method was not used in our study.

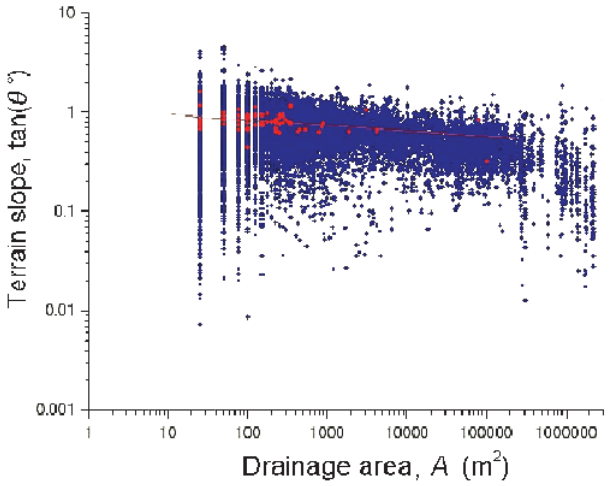

Fig. 11 Log-log plot between terrain slope and upstream drainage area. Blue dots indicate all no-landslide cells. Red dots are at the center of the landslide cells.

4. 2 Method of landslide susceptibility classification

To map landslide susceptibility, the relation between the two parameters was investigated in detail. In Fig. 12, the gray dots show landslide cells and black dots show non-landslide cells. The number of the gray dots was 5,421 and the number of the black dots was 121,927. Total number of the cells was 127,348. There are 90 landslides in the study area, and the average number of cells in the landslides is 60.2. In the log-log plot shown in Fig. 12, gray and black dots are overlapped. In order to map the landslide susceptibility, the landslide density was calculated and classified into four categories. The method is as follows.

The mean value and standard deviation of the terrain slope in the total 127,348 cells are 0.597 and 0.314, respectively. The histogram of the terrain slope is shown in Fig. 13. By using the mean value and the half standard deviation, the terrain slope was separated into eight classes, as follows: 0.001-0.282, 0.282-0.44, 0.44-0.597, 0.597-0.754, 0.754-0.911, 0.911-1.069, 1.069-1.226, and 1.226-10.

We also tried to separate the upstream drainage area in the total 127,348 cells by the mean value and half standard deviation method, but the number of the cells remarkably increases downstream. In this case, the upstream drainage area was separated into six classes, as follows: 10-100m^2, 100-1,000m^2, 1,000-10,000m^2, 10,000-100,000m^2, 100,000-1,000,000m^2, and 1,000,000-10,000,000m^2. The histogram of the upstream drainage area is shown in Fig. 14.

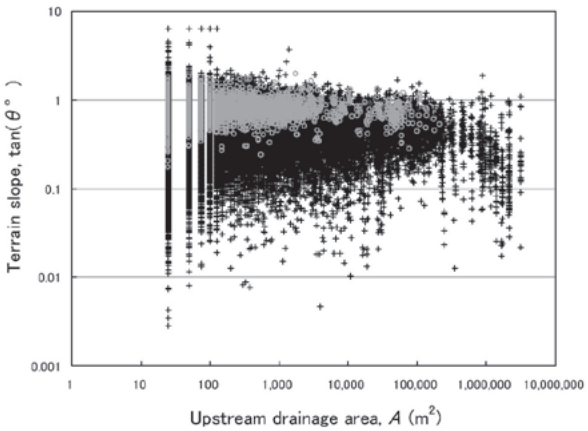

Fig. 12 Log-log plot between terrain slope and upstream drainage area. Black dots indicate all non-landslide cells. Gray dots are all landslide cells.

The eight classes by the six classes yielded 48 sections, the landslide density was calculated in each section, and landslide susceptibility was classified based on the density. Recently, Guzzetti et al. (1999) reviewed current techniques for landslide hazard evaluation. Their study classified techniques into the items shown below.

–Qualitative methods

–Quantitative methods

Indirect methods

1) Analysis of landslide inventories

2) Heuristic or index based method

3) Functional, statistically based models

Direct methods

4) Geo-technically or physically based models

The method applied in our study belongs to category 3.

5. Results and discussion

Table 3 shows the landslide density calculated in each section. The histogram of the landslide density, which is based on the Table 3, is shown in Fig. 15. In this figure, the landslide density is plotted as the ordinate and the ID number is plotted as the abscissa, whose number coincides with the ID number in the Table 3.

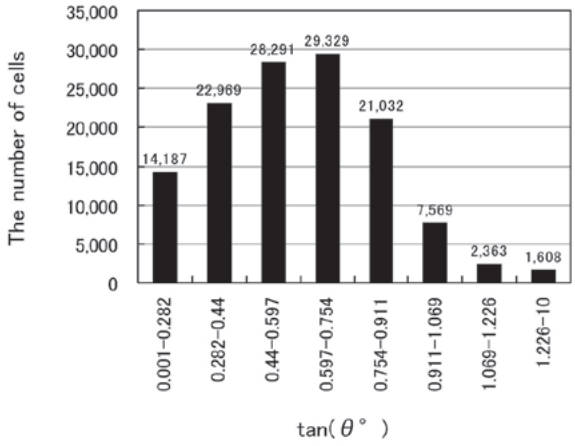

Fig. 13 The histogram of the terrain slope in each section.

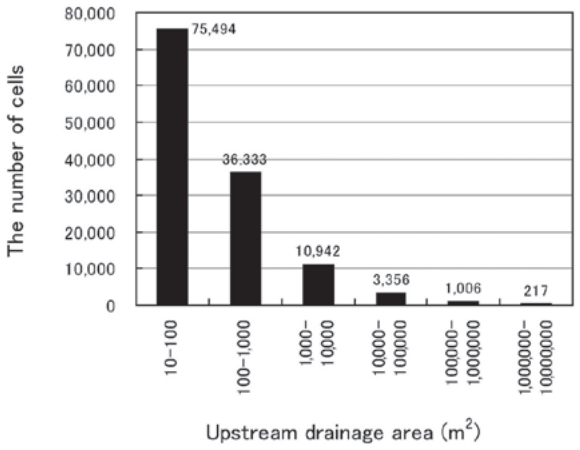

Fig. 14 The histogram of the upstream drainage area.

In Fig. 15, many ID numbers are concentrated in the two groups, from 0-5 % and >5 %. Considering the number of the cells (Table 3), the ID number 7 (landslide density: 0.27 %) has 12,212 cells, which occupies relatively many cells in the 0-5 % range. The ID number 25 (landslide density: 10.12 %) has 11,496 cells, which also occupies relatively many cells in the >5 % range. To describe these characteristic ID numbers in landslide susceptibility map separately, the main two groups of landslide density were subdivided into four categories, very low: 0-1 % (37,177 cells, 29.2 % of the watershed in area), low: 1-5 % (28,285 cells, 22.2 %), high: 5-10 % (32,540 cells, 25.6 %), and very high: >10 % (29,346 cells, 23.0 %).

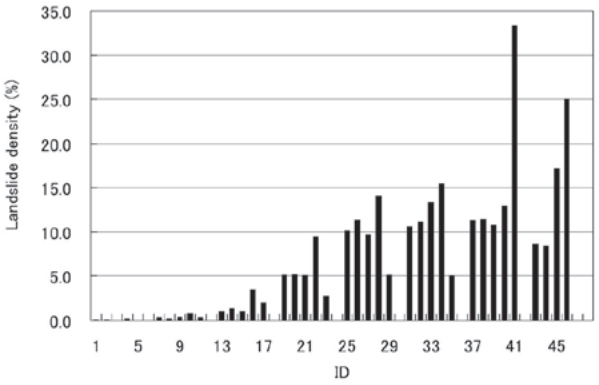

Fig. 15 The histogram of the landslide density.

Fig. 16 shows the result of landslide susceptibility mapping based on the four categories. Most upstream gentle slope areas, which are located at, for example, 1,020 m, 1,150 m, and 1,110 m in elevation (Fig. 3) fall into the very low susceptibility zone, and the slopes incised and eroded by gullies and valleys, which are located at, for example, 980 m and 755 m in elevation (Fig. 3) fall into the high susceptibility zone. This indicates that terrain slope played an important role in this study's classification. The valley bottom near the outlet of the watershed (Fig. 3) also falls into the very low susceptibility zone. A low susceptibility zone exists on the boundary between very low and high susceptibility zones, which seem to be located in the convex breaks of slopes.

According to our field survey, the land use of the very low susceptibility zones at 1,020 m, 1,150 m, and 1,110 m elevation (Fig. 3) is artificially planted needle-leaf evergreen forest, while deciduous shrubs and annual grasses mainly cover the high and very high susceptibility zones at 980 m and 755 m in elevation (Fig. 3) along the gullies and valleys. It is surmised that even if the needle-leaf evergreen trees were to be planted in high and very high susceptibility zones, they would still be destroyed by landslides, and such zones are not suitable for forestry.

Table 3 Calculated landslide densities.

ID	Terrain slope (tan θ °)	Upstream drainage area (m^2)	The number of grid points			Landslide density (%)
			Total	Landslide (a)	Non-landslide (b)	a/(a+b)
1	0.001–0.282	10–100	7695	6	7689	0.08
2		100–1000	4179	2	4177	0.05
3		1000–10000	1364	0	1364	0.00
4		10000–100000	584	1	583	0.17
5		100000–1000000	196	0	196	0.00
6		1000000–10000000	169	0	169	0.00
7	0.282–0.44	10–100	12212	33	12179	0.27
8		100–1000	7368	15	7353	0.20
9		1000–10000	2151	8	2143	0.37
10		10000–100000	869	7	862	0.81
11		100000–1000000	339	1	338	0.29
12		1000000–10000000	30	0	30	0.00
13	0.44–0.597	10–100	14904	150	14754	1.01
14		100–1000	9637	124	9513	1.29
15		1000–10000	2616	26	2590	0.99
16		10000–100000	871	30	841	3.44
17		100000–1000000	257	5	252	1.95
18		1000000–10000000	6	0	6	0.00
19	0.597–0.754	10–100	15609	806	14803	5.16
20		100–1000	10381	543	9838	5.23
21		1000–10000	2577	131	2446	5.08
22		10000–100000	612	58	554	9.48
23		100000–1000000	146	4	142	2.74
24		1000000–10000000	4	0	4	0.00
25	0.754–0.911	10–100	11496	1163	10333	10.12
26		100–1000	7566	860	6706	11.37
27		1000–10000	1635	158	1477	9.66
28		10000–100000	292	41	251	14.04
29		100000–1000000	39	2	37	5.13
30		1000000–10000000	4	0	4	0.00
31	0.911–1.069	10–100	4237	448	3789	10.57
32		100–1000	2622	290	2332	11.06
33		1000–10000	591	79	512	13.37
34		10000–100000	97	15	82	15.46
35		100000–1000000	20	1	19	5.00
36		1000000–10000000	2	0	2	0.00
37	1.069–1.226	10–100	1385	157	1228	11.34
38		100–1000	763	87	676	11.40
39		1000–10000	176	19	157	10.80
40		10000–100000	31	4	27	12.90
41		100000–1000000	6	2	4	33.33
42		1000000–10000000	2	0	2	0.00
43	1.226–10	10–100	1079	93	986	8.62
44		100–1000	442	37	405	8.37
45		1000–10000	76	13	63	17.11
46		10000–100000	8	2	6	25.00
47		100000–1000000	3	0	3	0.00
48		1000000–10000000	0	0	0	–
			127348	5421	121927	

6. Conclusion

In this study, precise DTM whose discrepancy between two measurements was 0.05 m in the X direction, -0.04 m in Y, and -0.01 m in Z was measured by airborne LIDAR. The five-meter-grid DTM was produced by interpolation of random points of DTM.

Terrain slope and upstream drainage area were investigated in each cell. The two parameters were combined and 48 sections were assigned. Using the landslide inventory map, the landslide density was calculated in each section. Based on the latter, the watershed in the study area was classified into the four landslide susceptibility classes; very low: 0-1 % (29.2 % of the watershed in the area), low: 1-5 % (22.2 %), high: 5-10 % (25.6 %), and very high: >10 % (23.0 %). The landslide susceptibility was mapped based on the four categories, and it is believed to be able to predict the severiy of disaster in the study area.

Acknowledgements

This study was carried out as part of the "Study on the Mechanism and Areal Prediction of Earthquakes and Rainfall- Induced Rapid and Long-Traveling Flow-Phenomena (APERIF)". It was funded by the Special Coordination Fund for the Promotion of Science and Technology, granted by the Ministry of Education, Culture, Sports, Science and Technology of Japan (MEXT).

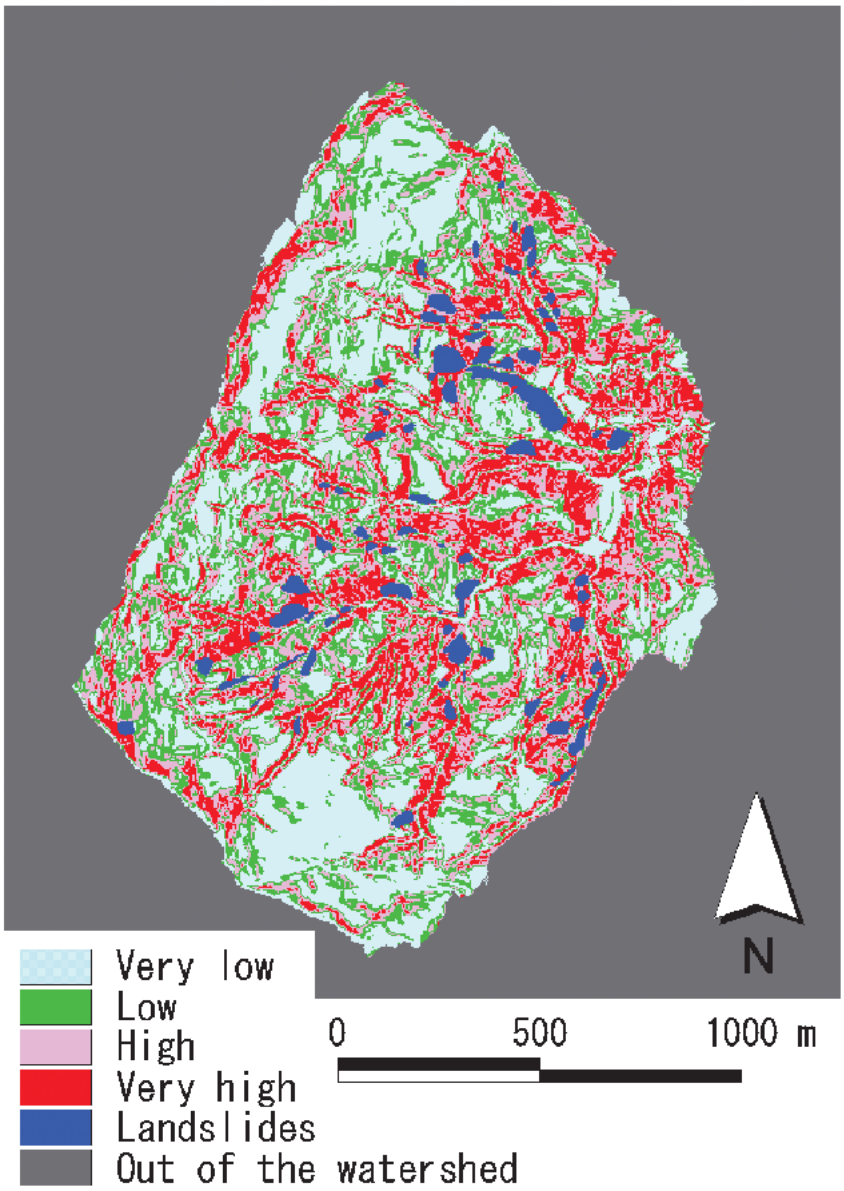

Fig. 16 Landslide susceptibility map of the study area.

References

Ackermann, F. (1999): Airborne laser scanning – present status and future expectations. ISPRS Journal of Photogrammetry and Remote Sensing 54, 64–67.

Fukuoka, H., Sassa, K., Scarascia-Mugnozza, G. (1997) : Distribution of landslides triggered by the 1995 Hyogoken-Nanbu earthquake and long run-out mechanism of the Takarazuka golf course landslide. Journal of Physics of the Earth, 45, 83-90.

Guzzetti, F., Carrara, A., Cardinali, M., Reichenbach, P. (1999): Landslide hazard evaluation: a review of current techniques and their application in a

multi-scale study, central Italy. Geomorphology 31, 181–216.

Hasegawa, H., Okamatsu, K. (2001): Detailed landform feature and characteristics extraction with high dense DTM data. Proceedings of the autumn conference of the Japan society of photogrammetry and remote sensing, pp.189–192. (in Japanese)

Hatano, S. (1974): Topography caused by rapid mass movement (part II). Tsuchi to Kiso, Japanese Geotechnical Society 22 (11), 85–93. (in Japanese)

Hutchinson, J.N. (1988): General report: Morphological and geotechnical parameters of landslides in relation to geology and hydrogeology. In: Bonnard, C. (Ed.), Landslides, A.A.Balkema, Rotterdam, Netherlands, pp.3-35.

Lee, S., Chwae, U., Min, K. (2002): Landslide susceptibility mapping by correlation between topography and geological structure: the Janghung area, Korea. Geomorphology 46, 149-162.

Lee, S., Ryu, J.H., Min, K., Won, J.S. (2003): Landslide susceptibility analysis using GIS and artificial neural network. Earth Surface Processes and Landforms 28, 1361-1376.

Masaharu, H., Hasegawa, H., Ohtsubo, K. (2001): Three-dimensional city modeling from airborne laser scanning. Proceedings of the 20th International Cartographic Conference, Vol. 2, International Cartographic Association, Beijing, China, pp.1337–1343.

McKean, J., Roering, J. (2004): Objective landslide detection and surface morphology mapping using high-resolution airborne laser altimetry, Geomorphology 57, 331-351.

Ohmori, H. (2000): Morphotectonic evolution of Japan. In: M. A. Summerfield (Ed.), Geomorphology and global tectonics, John Wiley & Sons, Chichester, UK, pp.147–166.

Raber, G. T., Jensen, J. R., Schill, S. R., Schuckman, K. (2002): Creation of digital terrain models using an adaptive lidar vegetation point removal process. Photogrammetric Engineering and Remote Sensing 68, 1307–1315.

Sassa, K., Fukuoka, H., Wang, G., Ishikawa, N. (2004): Undrained dynamic-loading ring-shear apparatus and its application to landslide dynamics. Landslides, 1, 7-19.

Sato, H.P., Hasegawa, H., Okamatsu, K., Masaharu, H. (2002): Landslide topography measurement by airborne laser scanning. Proceedings of International Symposium on Landslide Risk Mitigation and Protection of Cultural and Natural Heritage, UNESCO and Kyoto University, Kyoto, Japan, pp.375-383.

Sekiguchi, T., Sato, H.P. (2004): Mapping of micro topography using airborne laser scanning, Landslides, 1, 195-202.

Varnes, D.J. (1978): Slope movement types and processes. In: Schuster, R.L. and Krizek, R.J. (Eds.), Landslide: analysis and control, Transportation Research Board special report 176, National Academy of Science, Washington, D.C., US, pp.11-33.

Wehr, A., Lohr, U. (1999): Airborne Laser Scanning – An Introduction and Overview. ISPRS Journal of Photogrammetry and Remote Sensing 54, 68–82.